

We are IntechOpen, the world's leading publisher of Open Access books Built by scientists, for scientists

6,900

Open access books available

186,000

International authors and editors

200M

Downloads

Our authors are among the

154

Countries delivered to

TOP 1%

most cited scientists

12.2%

Contributors from top 500 universities



WEB OF SCIENCE™

Selection of our books indexed in the Book Citation Index
in Web of Science™ Core Collection (BKCI)

Interested in publishing with us?
Contact book.department@intechopen.com

Numbers displayed above are based on latest data collected.
For more information visit www.intechopen.com



A Fully Discrete SIPG Method for Solving Two Classes of Vortex Dominated Flows

Lunji Song

Abstract

To simulate incompressible Navier–Stokes equation, a temporal splitting scheme in time and high-order symmetric interior penalty Galerkin (SIPG) method in space discretization are employed, while the local Lax-Friedrichs flux is applied in the discretization of the nonlinear term. Under a constraint of the Courant–Friedrichs–Lewy (CFL) condition, two benchmark problems in 2D are simulated by the fully discrete SIPG method. One is a lid-driven cavity flow and the other is a circular cylinder flow. For the former, we compute velocity field, pressure contour and vorticity contour. In the latter, while the von Kármán vortex street appears with Reynolds number $50 \leq Re \leq 400$, we simulate different dynamical behavior of circular cylinder flows, and numerically estimate the Strouhal numbers comparable to the existing experimental results. The calculations on vortex dominated flows are carried out to investigate the potential application of the SIPG method.

Keywords: Navier–stokes equations, von Kármán vortex street, discontinuous Galerkin method, interior penalty

1. Introduction

The Navier–Stokes equations are a concise physics model of low Knudsen number (i.e. non-rarefied) fluid dynamics. Phenomena described with the Navier–Stokes equations include boundary layers, shocks, flow separation, turbulence, and vortices, as well as integrated effects such as lift and drag. Analytical solutions of real flow problems including complex geometries are not available, therefore numerical solutions are necessary. The Navier–Stokes equation has been investigated by many scientists conducting research on numerical schemes for approximation solutions (see [1–8]).

There exist two ways to provide reference data for such problems: One consists in the measurement of quantities of interest in physical experiments and the other is to perform careful numerical studies with highly accurate discretizations. With the prevalence and development of high-performance computers, advanced numerical algorithms are able to be tested for the validation of approaches and codes and for high-order convergence behavior of delicate discretizations.

Among discontinuous Galerkin (DG) methods, primal schemes and mixed methods are distinguished. The former depend on appropriate penalty terms of the discontinuous shape functions, while the latter rely on the mixed methods as the

original second-order or higher-order partial differential equations are written as a system of first order partial differential equations with designed suitable numerical fluxes. Interior penalty discontinuous Galerkin methods (IPDG) are known as the representative of primal schemes whereas local discontinuous Galerkin methods (LDG) belong to the class of mixed methods [9]. About IPDG, symmetric interior penalty Galerkin (SIPG) and non-symmetric interior penalty Galerkin (NIPG) methods were first introduced originally for elliptic problems by Wheeler [10] and Rivi re et al. [11]. Then, we presented some numerical analysis and simulations on nonlinear parabolic problems [12]. Recently, some work based on the SIPG and NIPG methods has been successfully applied to the steady-state and transient Navier–Stokes Equations [2, 13, 14], with careful analysis being conducted on optimal error estimates for the velocity.

The physics of Navier–Stokes flows are non-dimensionalized by Mach number M and Reynolds number Re ,

$$M = \frac{\mathbf{u}_\infty}{\mathbf{a}}, \quad (1)$$

$$Re = \frac{\rho \mathbf{u}_\infty D}{\mu}, \quad (2)$$

where ρ is the density of the fluid, and μ is the dynamic viscosity. The kinematic viscosity ν is the ratio of μ to ρ . At low Knudsen numbers, Navier–Stokes surface boundary conditions are effectively no-slip (i.e. zero velocity). Diffusion of momentum from freestream to surface no-slip velocities forms boundary layers decreasing in thickness as Reynolds number increases. Thus, the range of characteristic solution scale increases as the Reynolds number increases. Nonlinear convective terms coupled with the strong velocity gradients in the Navier Stokes equations drive fluid flow at even moderate Reynolds numbers to inherently unsteady behavior. Rotational flow is measured in terms of the vorticity ω , defined as the curl of a velocity vector \mathbf{v} ,

$$\omega = \nabla \times \mathbf{v} \quad (3)$$

The related concept of circulation Γ is defined as a contour integral of vorticity by

$$\Gamma = \oint_{\partial S} \mathbf{v} \cdot d\mathbf{s} = - \iint_S \omega \cdot \hat{\mathbf{n}} dS \quad (4)$$

The concept of a vortex is that of vorticity concentrated along a path [15].

Lid driven cavity flows are geometrically simple boundary conditions testing the convective and viscous portions of the Navier Stokes equation in an enclosed unsteady environment. The cavity flow is characterized by a quiescent flow with the driven upper lid providing energy transfer into the cavity through viscous stresses. Boundary layers along the side and lower surfaces develop as the Reynolds number increases, which tends to shift the vorticity center of rotation towards the center. A presence of the sharp corner at the downstream upper corner increasingly generates small scale flow features as the Reynolds number increases. Full cavity flows remain a strong research topic for acoustics and sensor deployment technologies.

For non-streamlined blunt bodies with a cross-flow, an adverse pressure gradient in the aft body tends to promote flow separation and an unsteady flow field. The velocity field develops into an oscillating separation line on the upper and lower surfaces. This manifests as a series of shed vortices forming and then convecting downstream with the mean flow. The von K rm n vortex street is named after the engineer and fluid

dynamicist Theodore Kármán (1963; 1994). Vortex streets are ubiquitous in nature and are visibly seen in river currents downstream of obstacles, atmospheric phenomena, and the clouds of Jupiter (e.g. The Great Red Spot). Shed vortices are also the primary driver for the zig-zag motion of bubbles in carbonated drinks. The bubble rising through the drink creates a wake of shed vorticity which impacts the integrated pressures causing side forces and thus side accelerations. The physics of sound generation with an Aeolians harp operates by alternating vortices creating harmonic surfaces pressure variations leading to radiated acoustic tones. Tones generated by vortex shedding are the so-called Strouhal friction tones. If the diameter of the string, or cylinder immersed in the flow is D and the free stream velocity of the flow is \mathbf{u}_∞ then the shedding frequency f of the sound is given by the Strouhal formula

$$St = \frac{fD}{\mathbf{u}_\infty}, \quad (5)$$

where $f = T^{-1}$, and St is the Strouhal number named after Vincent Strouhal, a Czech physicist who experimented in 1878 with wires experiencing vortex shedding and singing in the wind (Strouhal, 1878; White, 1999). The Strouhal formula provides an experimentally derived shedding frequency for fluid flow. Therefore, we are interested in an investigation of Stouhal numbers of incompressible flow at different Reynolds number.

Let Ω be a bounded polygonal domain in \mathbb{R}^2 . The dynamics of an incompressible fluid flow in 2D is described by the Navier–Stokes equations, which include the equations of continuity and momentum, written in dimensionless form [8] as follows:

$$\frac{\partial \mathbf{u}}{\partial t} - \nu \Delta \mathbf{u} + (\mathbf{u} \cdot \nabla) \mathbf{u} + \nabla p = \mathbf{f}, \quad \text{in } \Omega \times (0, T) \quad (6)$$

$$\nabla \cdot \mathbf{u} = 0, \quad \text{in } \Omega \times (0, T) \quad (7)$$

$$\mathbf{u}|_{t=0} = \mathbf{u}_0, \quad (8)$$

subject to the boundary conditions on $\partial\Omega$:

$$\alpha \mathbf{u} + (1 - \alpha) \frac{\partial \mathbf{u}}{\partial \mathbf{n}} = \mathbf{u}_\infty.$$

Here the parameter α has the limit values of 0 for the free-slip (no stress) condition (Neumann) and 1 for the no-slip condition (Dirichlet); $\mathbf{u} = (u, v)$ is the velocity; t is the time; and p is the pressure. In general, the external force \mathbf{f} is not taken into account in Eq. (6).

Using the divergence free constraint, problem (6)–(8) can be rewritten in the following conservative flux form [16]:

$$\frac{\partial \mathbf{u}}{\partial t} - \nu \Delta \mathbf{u} + \nabla \cdot \mathbf{F} + \nabla p = \mathbf{f}, \quad \text{in } \Omega \times (0, T) \quad (9)$$

$$\nabla \cdot \mathbf{u} = 0, \quad \text{in } \Omega \times (0, T) \quad (10)$$

$$\mathbf{u}|_{t=0} = \mathbf{u}_0, \quad (11)$$

with the flux F being defined as

$$F(\mathbf{u}) = \mathbf{u} \otimes \mathbf{u} = \begin{bmatrix} u^2 & uv \\ uv & v^2 \end{bmatrix}. \quad (12)$$

and $\mathbf{u} \otimes \mathbf{v} = u_i v_j, i, j = 1, 2$. Indeed, it holds

$$\mathcal{N}(\mathbf{u}) = \begin{pmatrix} \frac{\partial(u^2)}{\partial x} + \frac{\partial(uv)}{\partial y} \\ \frac{\partial(uv)}{\partial x} + \frac{\partial(v^2)}{\partial y} \end{pmatrix} = \nabla \cdot F(\mathbf{u}).$$

A locally conservative DG discretization will be employed for the Navier–Stokes Eq. (9)–(11). We denote by \mathcal{E}_h a shape-regular triangulation of the domain $\bar{\Omega}$ into triangles, where h is the maximum diameter of elements. Let Γ_h^I be the set of all interior edges of \mathcal{E}_h and Γ_h^B be the set of all boundary edges. Set $\Gamma_h = \Gamma_h^I \cup \Gamma_h^B$. For any nonnegative integer r and $s \geq 1$, the classical Sobolev space on a domain $E \subset \mathbb{R}^2$ is

$$W^{r,s}(E) = \{v \in L^s(E) : \forall |m| \leq r, \partial^m v \in L^s(E)\}.$$

We define the spaces of discontinuous functions

$$V = \{\mathbf{v} \in L^2(\Omega)^2 : \forall E \in \mathcal{E}_h, \mathbf{v}|_E \in (W^{2,4/3}(E))^2\},$$

$$M = \{q \in L^2(\Omega) : \forall E \in \mathcal{E}_h, q|_E \in W^{1,4/3}(E)\}.$$

The jump and average of a function ϕ on an edge e are defined by:

$$[\phi] = (\phi|_{E_k})|_e - (\phi|_{E_l})|_e,$$

$$\{\phi\} = \frac{1}{2} \left((\phi|_{E_k})|_e + (\phi|_{E_l})|_e \right).$$

Further, let \mathbf{v} be a piecewise smooth vector-, or matrix-valued function at $\mathbf{x} \in e$ and denote its jump by

$$[\mathbf{v}] := \mathbf{v}^+ \cdot \mathbf{n}_{E^+} + \mathbf{v}^- \cdot \mathbf{n}_{E^-},$$

where e is shared by two elements E^+ and E^- , and an outward unit normal vector \mathbf{n}_{E^+} (or \mathbf{n}_{E^-}) is associated with the edge e of an element E^+ (or E^-). The tensor product of two tensors \mathbf{T} and \mathbf{S} is defined as $\mathbf{T} : \mathbf{S} = \sum_{ij} T_{ij} S_{ij}$.

Let $\mathbb{P}_N(E)$ be the set of polynomials on an element E with degree no more than N . Based on the triangulation, we introduce two approximate subspaces $\mathbf{V}_h(\subset V)$ and $M_h(\subset M)$ for integer $N \geq 1$:

$$\mathbf{V}_h = \left\{ \mathbf{v} \in L^2(\Omega)^2 : \forall E \in \mathcal{E}_h, \mathbf{v}_h \in (\mathbb{P}_N(E))^2 \right\},$$

$$M_h = \{q \in L^2(\Omega) : \forall E \in \mathcal{E}_h, q \in \mathbb{P}_{N-1}(E)\}.$$

We mainly cite the content of [17], in which was motivated by the work of Girault, Rivi re and Wheeler in a series of papers [2, 14]. Some projection methods [6, 18] have been developed to overcome the incompressibility constraints $\nabla \cdot \mathbf{u} = 0$. An implementation of the operator-splitting idea for discontinuous Galerkin elements was developed in [2]. We appreciate the advantages of the discontinuous Galerkin methods, such as local mass conservation, high order of approximation, robustness and stability. In this work, we will make use of the underlying physical nature of incompressible flows in the literature and extend the interior penalty discontinuous

Galerkin methods to investigate dynamical behavior of vortex dominated lid-driven and cylinder flows.

The chapter is organized following [17]. In Section 2, a temporal discretization for the Navier–Stokes equation is listed with operator-splitting techniques, and subsequently, the nonlinear term is linearized. Both pressure and velocity field can be solved successively from linear elliptic and Helmholtz-type problems, respectively. In Section 3, a local numerical flux will be given for the nonlinear convection term and an SIPG scheme will be used in spacial discretization for those linear elliptic and Helmholtz-type problems with appropriate boundary conditions, and in Section 4, simulation results are presented for a lid-driven cavity flow up to $Re = 7500$ and a transient flow past a circular cylinder, while numerical investigation on the Strouhal-Reynolds-number has been done, comparable to the experimental values from physics. Finally, Section 5 concludes with a brief summary.

2. Temporal splitting scheme

We consider here a third-order time-accurate discretization method at each time step by using the previous known velocity vectors. Let Δt be the time step, $M = \frac{T}{\Delta t}$, and $t_n = n\Delta t$. The semi-discrete forms of problem (6)–(8) at time t_{n+1} is

$$\frac{\gamma_0 \mathbf{u}^{n+1} - \alpha_0 \mathbf{u}^n - \alpha_1 \mathbf{u}^{n-1} - \alpha_2 \mathbf{u}^{n-2}}{\Delta t} - \nu \Delta \mathbf{u}^{n+1} + \nabla p^{n+1} \quad (13)$$

$$= -\beta_0 \mathcal{N}(\mathbf{u}^n) - \beta_1 \mathcal{N}(\mathbf{u}^{n-1}) - \beta_2 \mathcal{N}(\mathbf{u}^{n-2}) + \mathbf{f}(t_{n+1}),$$

$$\nabla \cdot \mathbf{u}^{n+1} = 0, \quad (14)$$

which has a timestep constraint based on the CFL condition (see [19]):

$$\Delta t \approx O\left(\frac{\mathcal{L}}{\mathcal{U}N^2}\right),$$

where \mathcal{L} is an integral length scale (e.g. the mesh size) and \mathcal{U} is a characteristic velocity. Because the semi-discrete system (13)–(14) is linearized, thus, a time-splitting scheme can be applied naturally, i.e., the semi-discretization in time (13)–(14) can be decomposed into three stages as follows.

- The first stage

When \mathbf{u}^n and \mathbf{u}^{n-1} ($n \geq 1$) are known, the following linearized third-order formula can be used

$$\frac{\gamma_0 \tilde{\mathbf{u}} - \alpha_0 \mathbf{u}^n - \alpha_1 \mathbf{u}^{n-1} - \alpha_2 \mathbf{u}^{n-2}}{\Delta t} = -\beta_0 \mathcal{N}(\mathbf{u}^n) - \beta_1 \mathcal{N}(\mathbf{u}^{n-1}) + \mathbf{f}(t_{n+1}) \quad (15)$$

with the following coefficients for the subsequent time levels ($n \geq 2$)

$$\gamma_0 = \frac{11}{6}, \quad \alpha_0 = 3, \alpha_1 = -\frac{3}{2}, \quad \alpha_2 = \frac{1}{3}, \quad \beta_0 = 2, \quad \beta_1 = -1.$$

Especially, by using the Euler forward discretization at the first time step ($n = 0$), we can get a medium velocity field \mathbf{u}^1 by

$$\frac{\mathbf{u}^1 - \mathbf{u}^0}{\Delta t} = -\mathcal{N}(\mathbf{u}^0) + \mathbf{f}(t_1),$$

and \mathbf{u}^2 by

$$\frac{\gamma_0 \mathbf{u}^2 - \alpha_0 \mathbf{u}^1 - \alpha_1 \mathbf{u}^0}{\Delta t} = -\beta_0 \mathcal{N}(\mathbf{u}^1) - \beta_1 \mathcal{N}(\mathbf{u}^0) + \mathbf{f}(t_2),$$

which adopts the following coefficients to construct a second-order difference scheme for the time level ($n = 2$) in (15)

$$\gamma_0 = \frac{3}{2}, \quad \alpha_0 = 2, \alpha_1 = -\frac{1}{2}, \quad \alpha_2 = 0, \quad \beta_0 = 2, \quad \beta_1 = -1.$$

Note that the coefficients in (15) are adjustable, but high-order time discrete schemes need to be verified with stability analysis.

- The second stage

The pressure projection is as follows

$$\gamma_0 \frac{\tilde{\mathbf{u}} - \tilde{\mathbf{u}}}{\Delta t} = -\nabla p^{n+1}. \quad (16)$$

To seek p^{n+1} such that $\nabla \cdot \tilde{\mathbf{u}} = 0$, we solve the system

$$-\Delta p^{n+1} = -\frac{\gamma_0}{\Delta t} \nabla \cdot \tilde{\mathbf{u}}, \quad (17)$$

with a Neumann boundary condition being implemented on the boundaries as

$$\begin{aligned} \frac{\partial p^{n+1}}{\partial \mathbf{n}} &= \mathbf{f}^{n+1} - \beta_0 \mathbf{n} \cdot \left(\frac{\partial \mathbf{u}^n}{\partial t} + \nabla \cdot F(\mathbf{u}^n) - \nu \Delta \mathbf{u}^n \right) \\ &\quad - \beta_1 \mathbf{n} \cdot \left(\frac{\partial \mathbf{u}^{n-1}}{\partial t} + \nabla \cdot F(\mathbf{u}^{n-1}) - \nu \Delta \mathbf{u}^{n-1} \right) \\ &\quad - \beta_2 \mathbf{n} \cdot \left(\frac{\partial \mathbf{u}^{n-2}}{\partial t} + \nabla \cdot F(\mathbf{u}^{n-2}) - \nu \Delta \mathbf{u}^{n-2} \right) := G_n. \end{aligned}$$

One can compute the vorticity $\omega^n = \nabla \times \mathbf{u}^n$ at time $t^n = n \cdot \Delta t$. Then we use p^{n+1} to update the intermediate velocity $\tilde{\mathbf{u}}$ by (16).

- The third stage is completed by solving

$$\gamma_0 \frac{\mathbf{u}^{n+1} - \tilde{\mathbf{u}}}{\Delta t} = \nu \Delta \mathbf{u}^{n+1},$$

which can be written as a Helmholtz equation for the velocity

$$-\Delta \mathbf{u}^{n+1} + \frac{\gamma_0}{\nu \Delta t} \mathbf{u}^{n+1} = \frac{\gamma_0}{\nu \Delta t} \tilde{\mathbf{u}}. \quad (18)$$

From the three stages given above, we notice that (15) in the semi-discrete systems is presented in a linearized and explicit process, moreover, (17) and (18)

are obviously a type of elliptic and Helmholtz problems at each time step as $n \geq 2$. We decouple the incompressibility condition and the nonlinearity, then the pressure and velocity semi-discretizations (17)–(18) will be formulated by the interior penalty discontinuous Galerkin methods in spacial discretizations in the next section.

3. The spatial discretizations

For spacial approximations, assume that piecewise polynomials of order N are employed, then the approximation space can be rewritten as $\mathbf{V}_h = \bigoplus_{k=1}^K \mathbb{P}_N(E_k)^2$. In the approximating polynomial space for the velocity or pressure restricted to each element, a high-order nodal basis can be chosen, consisting of Lagrange interpolating polynomials defined on a reference simplex introduced in [20, 21]. We let \mathbf{u} be approximated by $\mathbf{u}_h \in \mathbf{V}_h$ and adopt a suitable approximation for the term F , i.e., $F(\mathbf{u}) \approx F(\mathbf{u}_h)$, where $F(\mathbf{u}_h)$ also can be represented as the L^2 -projection of $F(\mathbf{u}_h)$ on each element of \mathcal{T}_h . Multiplying the nonlinear term by a test function $\mathbf{v}_h \in \mathbf{V}_h$, integrating over the computational domain, and applying integration by parts, we have

$$\int_{\Omega} (\nabla \cdot F) \cdot \mathbf{v}_h d\mathbf{x} = - \sum_{E_k} \int_{E_k} (F \cdot \nabla) \cdot \mathbf{v}_h d\mathbf{x} + \sum_{e \in \Gamma_h} \int_e \mathbf{n}_e \cdot [F \cdot \mathbf{v}_h] ds, \quad (19)$$

where the term $(F \cdot \nabla) \cdot \mathbf{v}_h$ equals to $F_{ij} \frac{\partial v_{hi}}{\partial x_j}$, for $i, j = 1, 2$ and the indexes i, j correspond to the components of the related vectors. On each edge $e \in \partial E_1 \cap \partial E_2$ shared by two elements, to ensure the flux Jacobian of purely real eigenvalues, we may define $\lambda_{E_1,e}^+, \lambda_{E_2,e}^-$ the largest eigenvalue of the Jacobians $\frac{\partial}{\partial \mathbf{u}} (F \cdot \mathbf{n}_e) \big|_{\bar{\mathbf{u}}_{E_1}}$ and $\frac{\partial}{\partial \mathbf{u}} (F \cdot \mathbf{n}_e) \big|_{\bar{\mathbf{u}}_{E_2}}$, respectively, where $\bar{\mathbf{u}}_{E_1}$ and $\bar{\mathbf{u}}_{E_2}$ are the mean values of u_h on the elements E_1 and E_2 , respectively. The global Lax-Friedrichs flux is generally more dissipative than the local Lax-Friedrichs flux, therefore, we primarily consider the local flux on each edge. Although the Lax-Friedrichs flux is perhaps the simplest numerical flux and often the most efficient flux, it is not the most accurate scheme. A remedy of the problem is to employ high-order finite elements. By replacing the integrand in the surface integral as

$$\mathbf{n}_e \cdot [F \cdot \mathbf{v}_h] = \mathbf{n}_e \cdot \{F\} \cdot [\mathbf{v}_h] + \frac{\lambda_e}{2} [\mathbf{u}_h] \cdot [\mathbf{v}_h],$$

with $\lambda_e = \max(\lambda_{E_1,e}^+, \lambda_{E_2,e}^-)$, one can get a DG discretization for the nonlinear term in (19) by the local Lax-Friedrichs flux.

For the pressure correction step (17) and the viscous correction step (18), we use the SIPG method to approximate the correction steps. Choosing the orthonormal Legendre basis and the Legendre-Gauss-Lobatto quadrature points gives a well-conditioned Vandermonde matrix and the resulting interpolation well behaved, which greatly simplifies the formulas. The C^0 continuity condition of the basis in the discontinuous Galerkin formulation is not required. Enforcing a weak continuity on the interior edges by a penalty term, we have for (17)

$$a(p_h^{n+1}, \phi_h) = L_p(\phi_h), \quad \phi \in M_h,$$

where

$$a(p_h^{n+1}, \phi_h) = \sum_{E_k \in \mathcal{E}_h} \int_{E_k} \nabla p_h^{n+1} \cdot \nabla \phi_h dx - \sum_{e_k \in \Gamma_h} \int_{e_k} \left\{ \frac{\partial p_h^{n+1}}{\partial \mathbf{n}} \right\} [\phi_h] ds \\ - \sum_{e_k \in \Gamma_h} \int_{e_k} \left\{ \frac{\partial \phi_h}{\partial \mathbf{n}} \right\} [p_h^{n+1}] ds + \sum_{e_k \in \Gamma_h} \frac{\sigma_e}{|e_k|^\beta} \int_{e_k} [p_h^{n+1}] [\phi_h] ds,$$

$$\text{and } L_p(\phi_h) = \sum_{E_k \in \mathcal{E}_h} \int_{E_k} \frac{\gamma_0}{\Delta t} \nabla \cdot \tilde{\mathbf{u}} \phi_h dx + \sum_{e_k \in \partial\Omega} \int_{e_k} \phi_h G_n.$$

In general, σ_e shall be chosen sufficiently large to guarantee coercivity, more accurately, the threshold values of σ_e in [22] are given for $\beta = 1$ in the above formula, which is referred to an SIPG scheme. Especially, as $\beta > 1$, the scheme is referred to an over-penalized scheme and the threshold values of σ_e are presented in [23, 24]. Analogously, the SIPG discretization for (18) is given by

$$a(\mathbf{u}_h^{n+1}, \mathbf{v}_h) + \frac{\gamma_0}{\nu \Delta t} (\mathbf{u}_h^{n+1}, \mathbf{v}_h)_\Omega = L_{\mathbf{u}}(\mathbf{v}_h), \quad \forall \mathbf{v}_h \in \mathbf{V}_h,$$

where

$$a(\mathbf{u}_h^{n+1}, \mathbf{v}_h) = \sum_{E_k \in \mathcal{E}_h} \int_{E_k} \nabla \mathbf{u}_h^{n+1} : \nabla \mathbf{v}_h d\mathbf{x} - \sum_{e_k \in \Gamma_h} \int_{e_k} \{ \nabla \mathbf{u}_h^{n+1} \} \mathbf{n} \cdot [\mathbf{v}_h] ds \quad (20)$$

$$- \varepsilon \sum_{e_k \in \Gamma_h} \int_{e_k} \{ \nabla \mathbf{v}_h \} \mathbf{n} \cdot [\mathbf{u}_h^{n+1}] ds + \sum_{e_k \in \Gamma_h} \frac{\sigma_e}{|e_k|^\beta} \int_{e_k} [\mathbf{u}_h^{n+1}] \cdot [\mathbf{v}_h] ds, \quad (21)$$

and

$$L_{\mathbf{u}}(\mathbf{v}_h) = \left(\frac{\gamma_0}{\nu \Delta t} \tilde{\mathbf{u}}_h, \mathbf{v}_h \right)_\Omega - \sum_{e_k \in \partial\Omega} \int_{e_k} \left(\varepsilon \nabla \mathbf{v}_h \cdot \mathbf{n}_e - \frac{\sigma_e}{|e_k|^\beta} \mathbf{v}_h \right) \mathbf{u}_0.$$

where $\beta = 1, \varepsilon = 1$. Note that the parameter ε can be 1, -1 , and 0, the scheme (20) becomes SIPG, NIPG and IIPG, respectively. The SIPG scheme exhibits a stiffness matrix with symmetric structure. As a DG method, the SIPG scheme has some attractive advantages of DG methods including high order hp -approximation, local mass conservation, robustness and accuracy of DG methods for models with discontinuous coefficients and easy implementation on unstructured grids, while the flexibility of p -adaptivity (different orders of polynomials might be used for different elements) in DG methods has become competitive for modeling a wide range of engineering problems.

4. Numerical results

We present a lid-driven flow problem to verify the efficiency and robustness of the interior penalty discontinuous Galerkin method, and then investigate a flow past a cylinder with walls or without a wall, as well as the relationship between the Strouhal number and the Reynold number. Throughout the section, time steps $\Delta t \leq 1E - 03$ are taken.

Example 1. The lid-driven boundary conditions are given by:

$$\begin{cases} u(x, 1) = 1; & u(1, y) = 0; & u(0, y) = 0; & u(x, 0) = 0; \\ v(x, 1) = 1; & v(1, y) = 0; & v(0, y) = 0; & v(x, 0) = 0. \end{cases}$$

Here the mesh size of the initial coarse grid is 0.2 and then it is uniformly refined three times with piecewise discontinuous elements being applied into the fully discrete SIPG approach.

The boundary condition at the vertex is a jump from zero velocity on the edge to a unit velocity on the upper edge. Nature prevents this singularity with a boundary layer forming along all walls, making the vertex velocity zero. It is reasonable to adopt adaptive meshes for solving those singularity problems. Here, we apply the semi-implicit SIPG method with approximation polynomials of order $N = 3$ in a locally refined mesh in **Figure 1** to solve the incompressible flow. In **Figure 2**, the velocity profiles of (u, v) through the geometric center of the cavity are plotted with $Re = 1000, 5000, 7500$ taken. From **Figures 3–5**, with different Reynolds numbers taken up to 7500, the vorticity field exhibits the expected characteristics of a driven cavity flow consisting of a region of vortical flow centrally located. Energy enters the cavity through the viscous boundary layer formed by velocity gradients on the upper driven edge. Convection distributes flow properties throughout the domain.

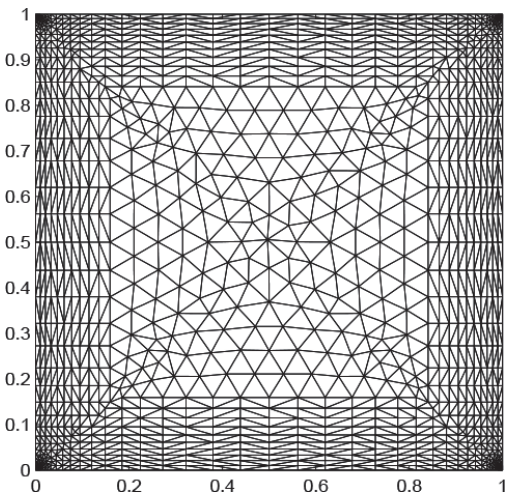


Figure 1.
An initial locally refined mesh.

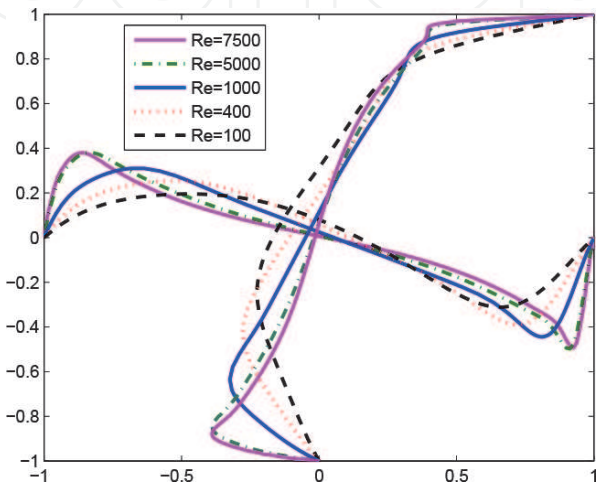


Figure 2.
Velocity profiles (u, v) through geometric center of the cavity for $Re = 100, 400, 1000, 5000, 7500$.

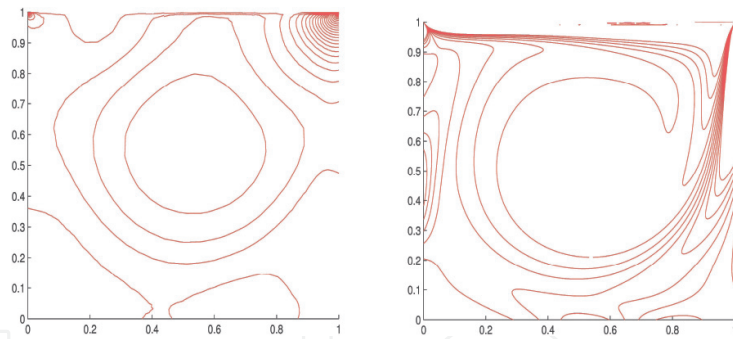


Figure 3.
 $Re = 1000$, $N = 4$, mesh #2. Left: pressure contour; right: vorticity contour.

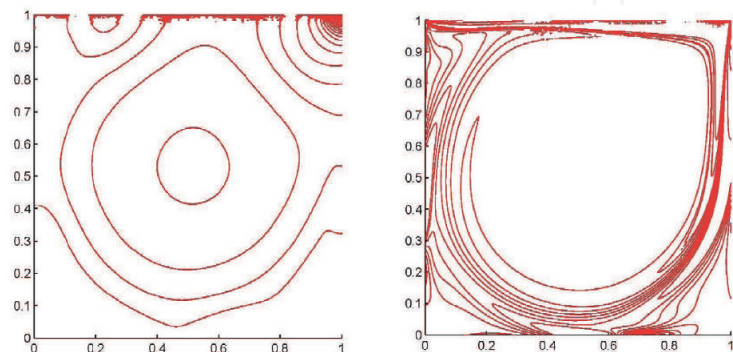


Figure 4.
 $Re = 5000$, $N = 3$, the initial mesh refined. Left: pressure contour; right: vorticity contour.

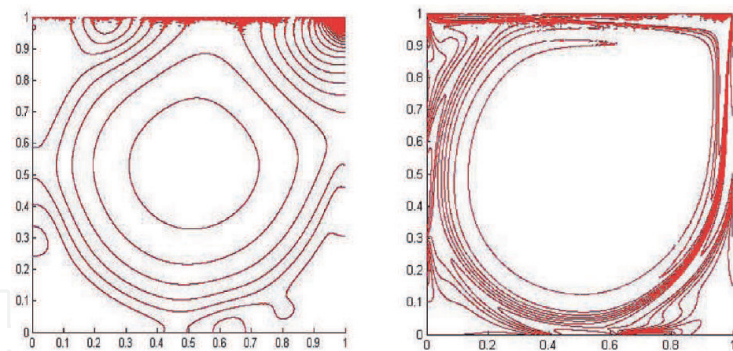


Figure 5.
 $Re = 7500$, $N = 3$, the initial mesh refined. Left: pressure contour; right: vorticity contour.

Moreover, a video on the dynamical evolution of vorticity isolines ($Re = 1000$, $N = 4$) can be browsed through a website (Available from: <https://youtu.be/UfGWvnoiW58>). These numerical simulations are performed for the Navier–Stokes equations which illustrate the effectiveness of the DG method.

Example 2. We simulate a channel flow past a circular cylinder with a radius 0.05 at the origin $(0, 0)$ for $Re = 100$ by the discontinuous Galerkin method in the domain $(-1, 3) \times (-0.5, 0.5)$. The free stream velocity on the inflow boundary is $\mathbf{u}_\infty = (1, 0)$, while the outflow boundary is $\frac{\partial \mathbf{u}}{\partial \mathbf{n}} = 0$. To the boundary conditions on the upper and lower sides, we present two different conditions for comparison (see **Figure 6**), which are wall ($u = 0, v = 0$) and homogeneous Neumann boundary conditions ($u = 1, \frac{\partial v}{\partial n} = 0$), respectively. The homogeneous Neumann boundary condition is a special non-reflecting case, where the boundary flux is zero. For reference, the density of the fluid is given by $\rho = 1 \text{ kg} \cdot \text{m}^{-3}$ and a locally refined mesh ($\max h = 0.088$) will be used for the simulations.

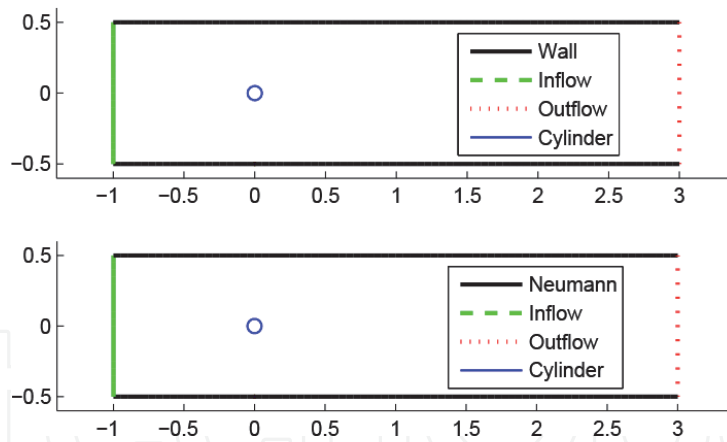


Figure 6.
Cylinder flow in a channel $N = 3$. Top: with walls; bottom: without a wall.

Cylinder flow contains the fundamentals of unsteady fluid dynamics in a simplified geometry. The flow properties and unsteadiness are well defined through years of experimental measurements across a wide range of Reynolds numbers [25], making the cylinder an ideal validation testcase for unsteady numerical fluid dynamics simulations.

Verification in a numerical domain requires insights from physics for a proper comparison to experimental and theoretical data. In **Figure 7**, we observe that the boundary layers forms along the upper and lower walls. From continuity of mass, the presence of a boundary layer decreasing the flow velocity near the wall requires an increase in the centerline average flow velocity. The cylinders wake provides a similar increase in centerline velocities. This implies a non-intuitive reality that drag can increase velocities within constrained domains. This effect is compensated for in wind tunnel test [26] environments topologically similar to **Figure 7** with a constant mass flow rate and no-slip walls. Drela [15] develops an analysis for 2D wind tunnels resulting in an effective coefficient of drag of

$$C_d = \left(1 - \frac{1}{2} \frac{c}{H} C_d - \frac{\pi}{2} \frac{A}{H^2}\right) C_{d_{un}},$$

and an effective Reynolds number of

$$Re = \left(1 + \frac{1}{4} \frac{c}{H} C_d + \frac{\pi}{6} \frac{A}{H^2}\right) Re_{un},$$

where the *un* subscript represents the uncorrected value, H represents the domain height, A represents the cylinder area and c represents the cylinder radius. Drelas analysis does not specifically include the boundary layer forming on the

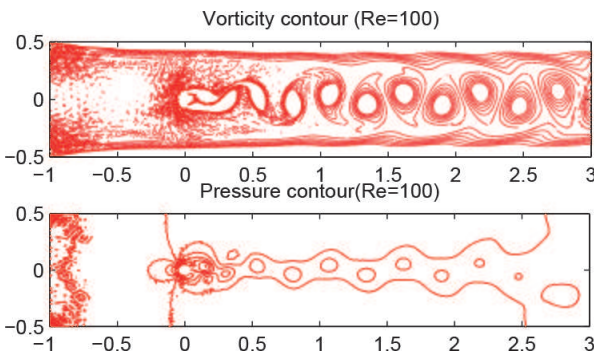


Figure 7.
Cylinder flow with walls, $Re = 100$. Top: vorticity contour; bottom: pressure contour.

upper and lower walls. The flow physics associated with wall boundary layer drag differs from cylinder drag in that the wall drag is a distributed effect of monotonically increasing drag with downstream distance rather than a conceptual point source of drag. The wall boundary layer tends to provide a steady acceleration of flow within the interior flow domain (i.e. non-boundary layer portion) leading to an effective buoyancy drag. A secondary feature of the wall boundary layer is that downstream flow features such as vortices are convected at a higher perturbation velocity compared to the initial upstream velocity. For numerical validation of raw experimental data, either the wind tunnel geometry should exactly match the numerical geometry, or the numerical geometry should be corrected using the concepts introduced above to match the actual wind tunnel geometry. Alternatively, the open-air corrected values should be used for validation. The above analysis provides insight into the domain height necessary to reduce volume blockage (c/H) and wake buoyancy (A/H^2) effects.

Alternatively, the flow without walls in **Figure 8** has no interference of the boundary layers along the channel on the up and bottom boundaries, thus the pressure contours expend after flow passing through the cylinder. We also compared the components of the velocity profiles along the x - direction in **Figure 9**, and observed that the boundary layers are produced in the top picture rather than in the bottom one. If the effect of the boundary layers disappeared, the velocity in the x - direction would reduce dispersively, in other words, the vortex lifespan is less than those produced in the channel with walls. The velocity profiles in the y - direction have been given in **Figure 10**.

We localize the domain around the cylinder and refine the mesh, then show the vorticity startup behavior in **Figure 11** as well as the pressure **Figure 12**. Upon startup, two vortices of opposite direction are formed on the upper and lower

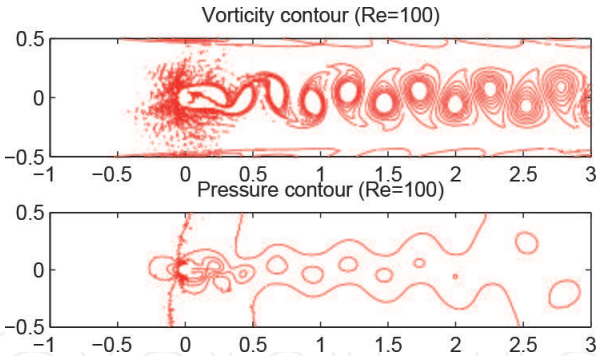


Figure 8. Flow past a cylinder in a channel without a wall, $Re = 100$. Above: vorticity contour; below: pressure contour.

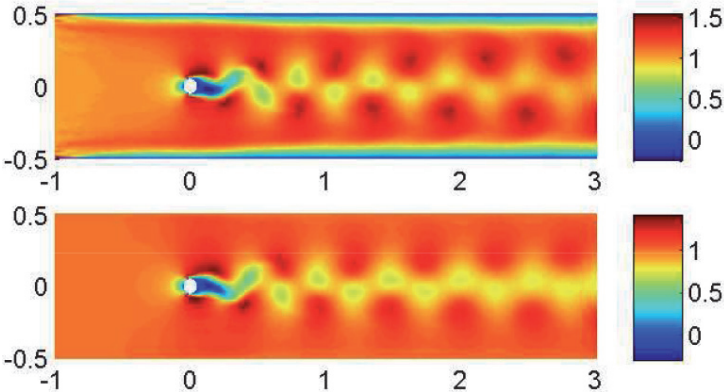


Figure 9. $Re = 100$. Above: velocity in x -direction with walls; below: velocity in x -direction without a wall.

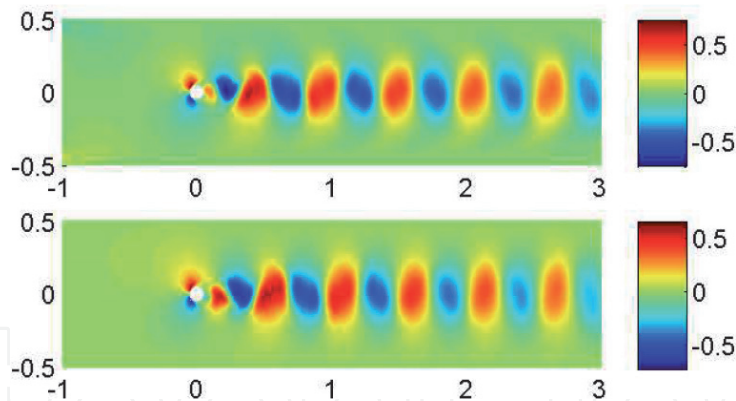


Figure 10.
Re = 100. Above: velocity in y-direction with walls; below: velocity in y-direction without a wall.

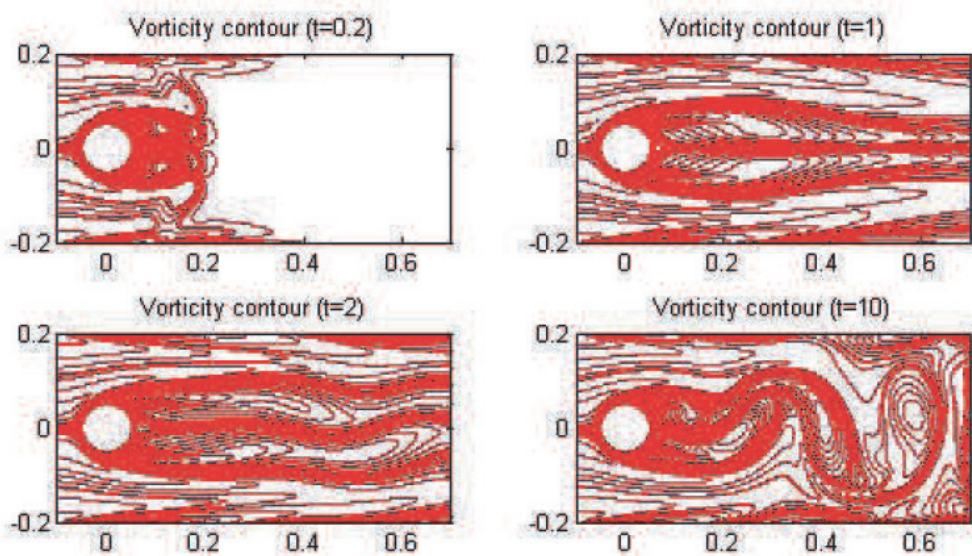


Figure 11.
Vorticity contours of flow past a cylinder without a wall at different time.

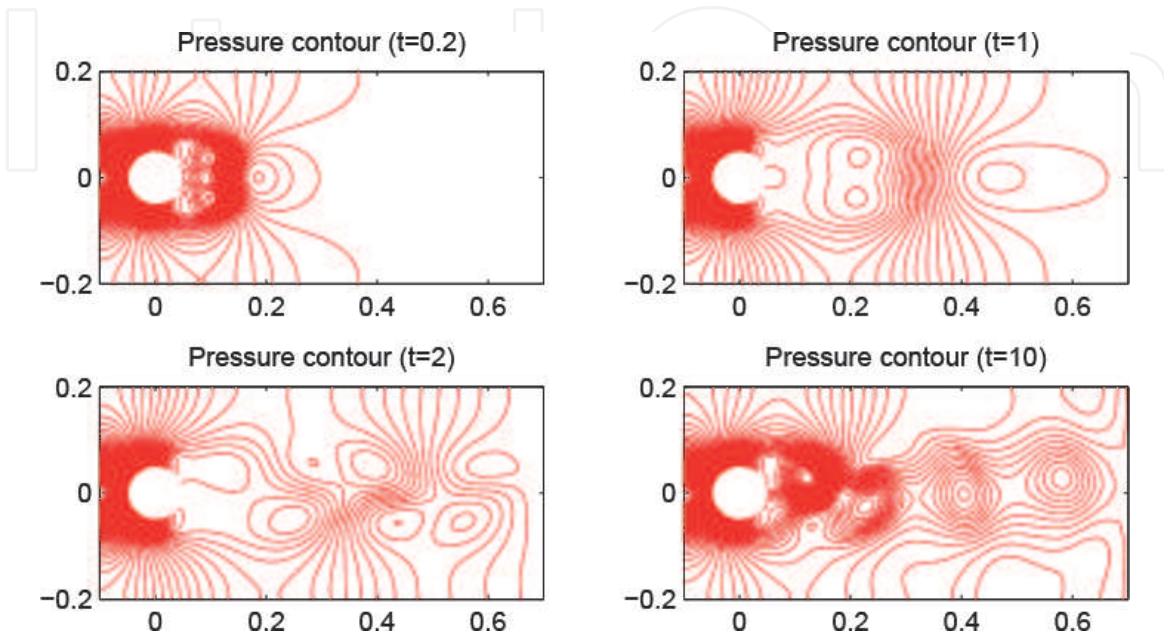


Figure 12.
Pressure contours of flow past a cylinder without a wall at different time.

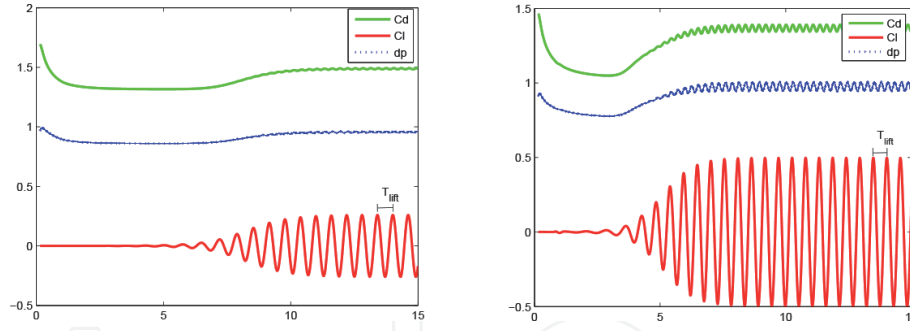


Figure 13.

Drag, lift coefficients and the variation of pressure with time, $Re = 80$ (left), $Re = 140$ (right).

aft portion of the cylinder. Given a low total simulation time, the flow field resembles the symmetrical low Reynolds number steady flow. As time progresses however, instabilities are magnified and the upper-lower symmetry increases. Given a total time of beyond $t = 10$, an autonomous and phased locked set of street vortices are generated. Surface pressures (**Figure 13** at $Re = 80, 140$) generated reflect the process, including a steady startup portion and the eventual vortex shedding frequency. Validation at $Re > 41$ requires sufficient time to obtain the unsteady behavior.

To reduce the effect of the boundary layers along the walls, the coefficients of drag and lift as well as the difference of pressure between the leading edge and the trailing edge on the cylinder shall be computed in a larger domain. Then in a domain $\Omega := [-1, 5] \times [-1, 1]$, higher order DG finite elements have been investigated. Based on the velocity \mathbf{u}_∞ and the diameter of the cylinder $D = 0.1$, we will chose different viscosity coefficients $\nu = 1e - 3, 5e - 4, 2.5e - 4$ etc. to simulate flow with different Reynolds numbers, that is, the cases $Re = 100, 200, 400$, respectively. Our interest is the drag coefficient C_d , the lift coefficient C_l on the cylinder and the difference of the pressure between the front and the back of the cylinder

$$d_p = p(t; -0.05, 0) - p(t; 0.05, 0).$$

We use the definition of C_d and C_l given in [4] as follows:

$$C_d = \frac{2}{\rho D u_{\max}^2} \int_S \left(\rho \nu \frac{\partial \mathbf{u}_{\mathbf{t}\mathbf{s}}(t)}{\partial \mathbf{n}} n_y - p(t) n_x \right) ds,$$

$$\text{and } C_l = -\frac{2}{\rho D u_{\max}^2} \int_S \left(\rho \nu \frac{\partial \mathbf{u}_{\mathbf{t}\mathbf{s}}(t)}{\partial \mathbf{n}} n_x + p(t) n_y \right) ds,$$

where $\mathbf{n} = (n_x, n_y)^T$ is the normal vector on the cylinder boundary S directing into Ω , $\mathbf{t}\mathbf{s} = (n_y, -n_x)^T$ the tangential vector and $\mathbf{u}_{\mathbf{t}\mathbf{s}}$ the tangential velocity along S . In the literature, Fey et al. in [27] propose the Strouhal number represented by piecewise linear relationships of the form

$$St = ST^* + \frac{m}{\sqrt{Re}}$$

with different values St^* and m in different shedding regimes of the 3D circular cylinder wake. We originally define the periodic T_{lift} of the lift coefficients (see **Figure 13**) by the periodic $T := \frac{1}{f}$ appearing in the definition of Strouhal number, i.e.,

$$St(Re) = \frac{D}{T_{lift} \mathbf{u}_\infty}, \quad (22)$$

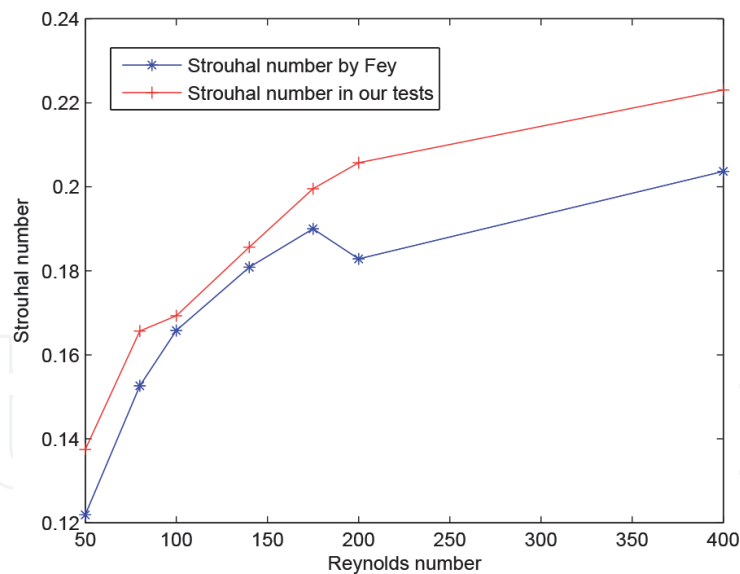


Figure 14.
 A comparison of Strouhal-Reynolds-number between our estimate and the linear fit in [27] for $50 \leq Re \leq 400$.

which comes from the classical definition (5). From the evolution of C_d , C_l and d_p as in **Figure 13**, we may find a period T_{lift} of the lift coefficients for different values of Re to calculate Strouhal number by (22). In **Figure 14**, a comparison of Strouhal numbers between the experimental estimates in Fey etc. [5] and our estimates from (22) indicates a behavioral match between the unsteady onset at approximately $Re = 50$ and the beginning of the transition to turbulence at $Re = 180$. Beyond $Re = 180$, the onset of turbulence changes the flow physics by drastically increasing the energy spectrum of the shed vorticity. The transition appears as a marked decrease in the Strouhal number prior to $Re = 200$. As the present SIPG solver does not include a 3D turbulence model, our estimates follow the laminar results into the actual turbulent region. Moreover, **Figure 14** verifies availability of the periodic of vortex street replaced by the periodic of the lift coefficients. There are many results for flow past a cylinder using Reynolds Averaged Navier–Stokes (RANS) method. For large Re up to 2000, the readers are referred to the reference [28] for details, for example, Strouhal number of a cylinder flow could experience a slight fall.

5. Conclusions

A SIPG solver is developed for the incompressible Navier Stokes equations of fluid flow. Two testcases are presented: a lid-driven cavity and a cylinder flow. The DG method produces stable discretizations of the convective operator for high order discretizations on unstructured meshes of simplices, as a requirement for real-world complex geometries. There are still some open problems, such as how the strouhal number of the von Kármán vortex street changes against the Reynolds number after oscillations or noises are added to the incident flow.

Acknowledgements

The author would like to thank INTECHOPEN for their fully sponsor the publication of this chapter and waive the Open Access Publication Fee completely.

Conflict of interest

The author declares no conflict of interest.

Abbreviations

IPDG	Interior penalty discontinuous Galerkin methods
SIPG	Symmetric interior penalty Galerkin method
NIPG	Non-symmetric interior penalty Galerkin method
CFL	Courant–Friedrichs–Lewy

Author details

Lunji Song
School of Mathematics and Statistics, Lanzhou University, Lanzhou, P.R. China

*Address all correspondence to: song@lzu.edu.cn

IntechOpen

© 2020 The Author(s). Licensee IntechOpen. This chapter is distributed under the terms of the Creative Commons Attribution License (<http://creativecommons.org/licenses/by/3.0>), which permits unrestricted use, distribution, and reproduction in any medium, provided the original work is properly cited. 

References

- [1] Shen J. On error estimates of the projection methods for the Navier-Stokes equations: Second-order schemes. *Math. Comp.* 1996; 65(215): 1039–1065.
- [2] Temam R. *Navier-Stokes Equations: Theory and Numerical Analysis*. Providence: AMS Chelsea publishing; 2001.
- [3] Castillo P, Cockburn B, Perugia I, and Schötzau D, An a priori error analysis of the local discontinuous Galerkin method for elliptic problems. *SIAM J. Numer. Anal.* 2000; 38: 1676–1706.
- [4] Karniadakis G, Sherwin SJ. *Spectral/hp element methods for CFD*. New York: Oxford University Press; 2005.
- [5] Hesthaven JS. From electrostatics to almost optimal nodal sets for polynomial interpolation in a simplex. *SIAM J. Numer. Anal.* 1998; 35(2): 655–676.
- [6] Hesthaven JS, Teng CH. Stable spectral methods on tetrahedral elements. *SIAM J. Sci. Comput.* 2000; 21: 2352–2380.
- [7] Barlow JB, Rae WH, Pope A. *Low-Speed Wind Tunnel Testing*. John Wiley; 1999.
- [8] Fey U, König M, Eckelmann H. A new Strouhal-Reynolds-number relationship for the circular cylinder in the range $47 \leq Re \leq 2 \times 10^5$. *Physics of Fluids*. 1998; 10(7): 1547–1549.
- [9] Ghia U, Ghia KN, Shin CT. High-Re solutions for incompressible flow using the Navier-Stokes equations and a multigrid method. *J. Comput. Phys.* 1982; 48: 387–411.
- [10] Kazim MNFM, Rasani R, Nuawi MZ, Harun Z, Hau YK, Majid MSA. Analysis of wake region behind bluff body for piezoelectric energy harvester. *J. Adv. Res. Fluid Mechan. Therm. Sci.* 2019; 55: 249–263.
- [11] Song L, O'Neill C. A high-order symmetric interior penalty discontinuous Galerkin scheme to simulate vortex dominated incompressible fluid flow, *AIMS Mathematics*, 2016; 1(1): 43–63.
- [12] Epshteyn Y, Rivière B. Estimation of penalty parameters for symmetric interior penalty Galerkin methods. *J. Comput. Appl. Math.* 2007; 206: 843–872.
- [13] Temam R. *Navier-Stokes Equations and Nonlinear Functional Analysis*, Volume 66 of CBMS-NSF Regional Conference Series in Applied Mathematics. Philadelphia: SIAM, 2nd edition, 1995.
- [14] Drela M. *Flight Vehicle Aerodynamics*. Boston: MIT Press; 2014.
- [15] Goyon O. High-Reynolds number solutions of Navier-Stokes equations using incremental unknowns. *Comput. Method. Appl. M.* 1996; 130: 319–335.
- [16] Schäfer M, Turek S. The benchmark problem ‘flow around a cylinder’, In *Flow Simulation with High-Performance Computers II*, Hirschel, E. H.(editor). Notes on Numerical Fluid Mechanics, vol. 52, Vieweg: Braunschweig; 1996. p. 547–566.
- [17] Hoerner SF. *Fluid-Dynamic Drag*, Bakersfield: Hoerner Fluid Dynamics; 1965.
- [18] Girault V, Rivière B, Wheeler MF. A splitting method using discontinuous Galerkin for the transient incompressible Navier-Stokes equations. *ESAIM: Mathematical*

Modelling and Numerical Analysis. 2005; 39(6): 1115–1147.

[19] Girault V, Rivi re B, Wheeler MF. A discontinuous Galerkin method with non-overlapping domain decomposition for the Stokes and Navier-Stokes problems. *Math. Comp.* 2005; 74: 53–84.

[20] Wheeler MF. An elliptic collocation-finite element method with interior penalties. *SIAM J. Numer. Anal.* 1978; 15: 152–161.

[21] Rivi re B, Wheeler MF, Girault V. Improved energy estimates for interior penalty, constrained and discontinuous Galerkin methods for elliptic problems. Part I. *Comput. Geosci.* 1999; 3: 337–360.

[22] Chorin AJ. On the convergence of discrete approximations to the Navier-Stokes equations. *Math. Comp.* 1969; 23: 341–353.

[23] Song L, Zhang Z. Polynomial preserving recovery of an over-penalized symmetric interior penalty Galerkin method for elliptic problems. *Discrete Contin. Dyn. Syst. – Ser. B* 2015; 20(5): 1405–1426.

[24] Song L, Zhang Z. Superconvergence property of an over-penalized discontinuous Galerkin finite element gradient recovery method. *J. Comput. Phys.* 2015; 299: 1004–1020.

[25] Song L, Gie GM, and Shiue MC. Interior penalty discontinuous Galerkin methods with implicit time-integration techniques for nonlinear parabolic equations. *Numer. Methods Partial Differential Equations.* 2013; 29(4): 1341–1366.

[26] Foias C, Manley O, Rosa R and Temam R. *Turbulence and Navier-Stokes equations.* Cambridge University Press; 2001.

[27] Shen J. Hopf bifurcation of the unsteady regularized driven cavity flow. *J. Comput. Phys.* 1991; 95: 228–245.

[28] Kaya S, Rivi re B. A discontinuous subgrid eddy viscosity method for the time-dependent Navier-Stokes equations. *SIAM J. Numer. Anal.* 2005; 43(4): 1572–1595.